JGR Solid Earth

RESEARCH ARTICLE
10.1029/2018JB016400

Transdimensional Bayesian Attenuation Tomography of the Upper Inner Core

Tanja Pejić[1,2], Rhys Hawkins[1], Malcolm Sambridge[1], and Hrvoje Tkalčić[1]

[1]Research School of Earth Sciences, The Australian National University, Canberra, ACT, Australia, [2]Now at Geoscience Australia, Canberra, ACT, Australia

Key Points:
- Transdimensional sampling of Voronoi cells on a spherical surface applied to a problem in global tomography
- No hemispherical pattern is observed in attenuation structure of the upper inner core
- The study provides a strong seismological hint for a strongly attenuating inner core

Supporting Information:
- Supporting Information S1

Correspondence to:
T. Pejić,
tanja.pejic@ga.gov.au

Citation:
Pejic, T., Hawkins, R., Sambridge, M., & Tkalčić, H. (2019). Transdimensional Bayesian attenuation tomography of the upper inner core. *Journal of Geophysical Research: Solid Earth*, *124*, 1929–1943. https://doi.org/10.1029/2018JB016400

Received 16 JUL 2018
Accepted 6 FEB 2019
Accepted article online 9 FEB 2019
Published online 16 FEB 2019

Abstract Following the linearized attenuation tomography from our previous study (Pejić et al., 2017, https://doi.org/10.1002/2016JB013692), we perform hierarchical transdimensional Bayesian tomography of the upper ≈ 400 km of the inner core, using 398 globally distributed t^* estimates. The results are in good agreement with the ones obtained through linearized tomography: they show more complex attenuation pattern than the purely hemispherical one, and the noise estimated from the hierarchical inversion is in good agreement with estimates obtained from the Discrepancy Principle in the previous study. The attenuation pattern we observe gives more weight to the geodynamical models that couple the thermal anomalies of the lowermost mantle to the inner core boundary.

1. Introduction

The inner core of the Earth is one of the few remaining research puzzles within deep Earth sciences. While our understanding of its structure and dynamics have improved over the last two decades, ongoing debates still allow for two or more scenarios of the inner core's dynamics that explain the observed seismic phenomena equally well. Pejić et al. (2017) provide a summary of recent findings and theories that were used to explain them and perform a linearized attenuation tomography using a data set of PKIKP and PKPbc phases. Seismic tomography is a common tool used in exploration of deep Earth structure and composition. Earth models are mostly parameterized as uniform cells in 2-D or 3-D, whose size and shape are fixed in advance. The size of the cells is a trade-off between the resolution and the uncertainty of the model; larger cells will yield smaller uncertainty at the expense of resolution (Backus & Gilbert, 1968). A major problem with seismic tomography is that it largely depends on the locations of sources (earthquake events) and receivers (seismic stations), both of which are unevenly distributed across the globe. The result is an irregular spatial distribution of information gathered in seismic tomography—while some regions will be traversed by a great number of seismic rays, others will have little or no information at all. As a consequence, imposing a regular global grid and a fixed number of parameters in tomographic studies will often result in introducing spurious artifacts in regions of low ray coverage, where the particular property being investigated is poorly constrained. This effect is usually mitigated by some form of regularization, for example, damping or smoothing. However, these methods are global in character, that is, they affect the entire model, so while averaging over large scales to suppress the overall effect of poorly covered regions, global regularization can completely mask small-scale features that could otherwise be resolved.

Seismologists have used irregular meshes in the past to work around this problem (Sambridge & Rawlinson, 2005, provide a review); however, in most of these studies the number of parameters is fixed in advance. Treating the number of unknown parameters as a parameter itself has received more attention in Earth sciences over the past decade. In this type of approach the parameterization is then determined by the data itself and the number of unknowns is a variable being inverted for by the tomographic algorithm.

In our previous study (Pejić et al., 2017), we have used probabilistic framework and least squares method to perform tomography of the upper inner core imposing a regular grid of 45° in size and two separate regularization techniques (damping and smoothing). Due to our irregular (and sparse in some regions) coverage of the upper inner core, this has, for example, resulted in an unrealistically high attenuation beneath South America. This is a good example of how global regularization can affect the results in a mixed-determined problem. Using smaller cells to better resolve the well-covered regions in our model would only amplify this problem, and the associated uncertainties would be even higher than those reported, while using larger cells

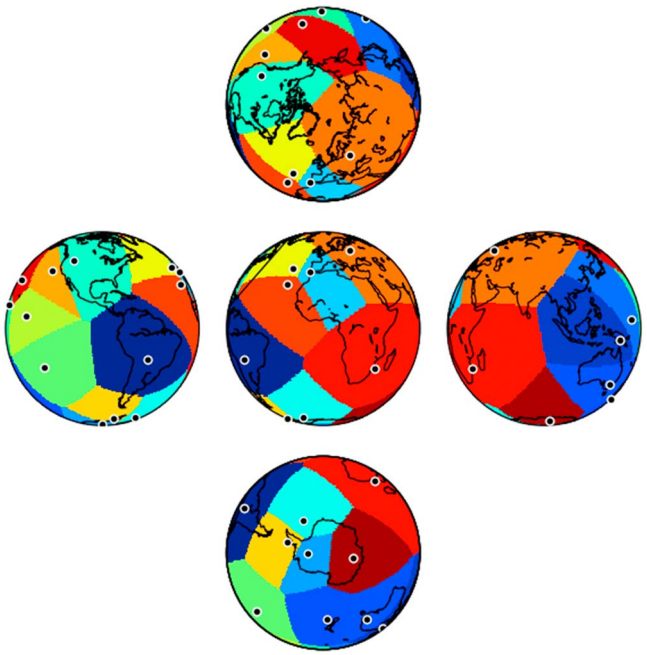

Figure 1. An example of Voronoi cells (in different colors) and their nodes (black circles) after a number of iterations of the transdimensional algorithm. The projection used allows to inspect the model from all perspectives including the polar ones.

would smooth out the results considerably and provide a false impression of the (good) resolution. These are the reasons why we decided to apply a transdimensional tomographic inversion to our problem.

1.1. Brief Overview of Transdimensional Methods

In a Bayesian formulation the inference is based on the so-called a posteriori probability distribution function of the unknown model parameters. It describes the probability of the model parameters given the observed data. Optimization schemes like the one used in Pejić et al. (2017) only provide a single model as a solution to the problem. This model is commonly an optimal set of parameters that maximize the fit of the predicted data to the observations (i.e., the likelihood function). Bayesian solutions, on the other hand, provide a whole ensemble of models, which may contain more information than just a single model. It allows for a more comprehensive assessment of model parameters and their uncertainties and calculation of common statistical quantities such as mode, mean, median, and variance, which can be computed from the ensemble of models. In transdimensional tomography the solution is an ensemble of models of differing parameterizations. It may seem that this would lead to highly complex models (with a large number of parameters) to provide the best data fit; however, a fundamental property of Bayesian inference is the so-called "natural parsimony," i.e., the preference for models of complexity that is sufficient to explain the observations. Given a choice between a simple and complex model that fits the data equally well, the simpler model will be preferred. This is because a more complex model (one with more free parameters) will, after normalization, have a lower predictive probability within the data range covered by both the complex and the simple models (Mackay, 2003; Sambridge et al., 2006).

In this study we show tomographic results using a transdimensional algorithm for the problem of attenuation in the upper inner core. Young et al. (2013) have previously modeled the lowermost mantle using Cartesian Voronoi cells. To account for periodicity over longitude, they have duplicated the data set and shifted it by 360°. In their approach the model space was defined on a flat projection and made to range between −360° and +360°, and once cropped to the range of −180° to +180° and wrapped around, the "seams" of the model would match. In this study, we use Voronoi cells on the surface of a sphere of uniform thickness, which we will refer to as the "spherical" Voronoi cells. The spherical Voronoi cells form an irregular mesh that directly partitions a spherical surface. Since the model is defined on the sphere, rather than a flat projection, this prevents distortion at the poles since there are no singularities as in the case of Cartesian approach. An example of Voronoi cells after a number of iterations is shown in Figure 1. The projection used in Figure 1 is a way of presenting variations of properties in the inner core from all perspectives, including the polar ones, because it was previously documented that the velocity and attenuation structure is hemispherical (see discussion of various geodynamical inner core models in section 7). Additionally, the idea of spatially averaging many piecewise Voronoi cells to produce a smooth field is discussed in detail in Bodin and Sambridge (2009) and illustrated in their Figure 8. We will use this projection to show our inverted attenuation models. Our algorithm is implementing Hierarchical Bayes transdimensional method (Bodin et al., 2012; Dettmer et al., 2010; Malinverno & Briggs, 2004) where the data noise is also treated as a parameter of the inversion. When the expectations of a posterior distribution are computed, all these models with variable geometries are overlapped to combine into one smooth solution with no need for explicit regularization (Bodin et al., 2012; Malinverno, 2002).

2. Data

The data set used is the same as the one shown in our previous study and will be presented briefly here, the reader is referred to Pejić et al. (2017) for full details. The simulated annealing *SAWIB* algorithm (Garcia et al., 2013) was used to estimate the t^* parameter for 398 waveforms of globally distributed earthquakes. The *SAWIB* algorithm performs a full synthetic waveform fit to observed waveforms for multiple records of a single earthquake. *SAWIB* optimizes multiple parameters until the best fit according to the simulated

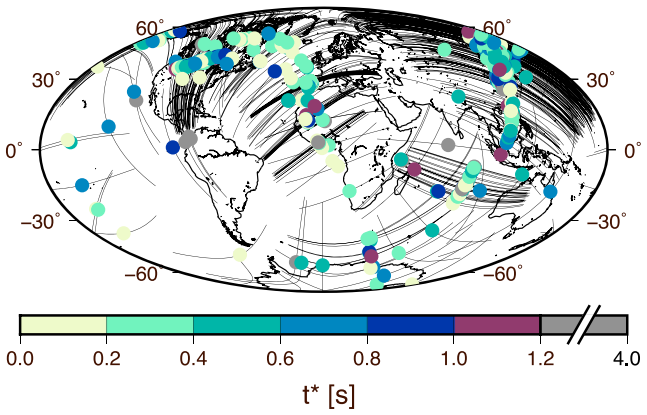

Figure 2. The t^* estimates obtained in this study. Black lines are portions of raypaths propagating through the inner core, and filled circles are t^* estimates plotted in the locations of the bottoming points of their respective raypaths. The range of the color scale has been adjusted to clearly show the majority of estimated t^* parameters and their variety. All estimates larger than 1.2 plot as gray filled circles (see text for explanation).

annealing algorithm is achieved. One of those parameters is the attenuation parameter t^*. The t^* parameter is a measure of attenuation, inversely proportional to quality factor Q. Its definition and application to the study of the inner core is further discussed in Pejić et al. (2017). The t^* quantity is assigned to the bottoming point of a particular PKP ray. We focused on the records that show clear PKP arrivals on unfiltered displacement seismograms, for events of magnitude between 5.5 and 7, and deeper than 100 km. We used only PKIKP and PKPbc phases, and the data set spans the epicentral distances between 147° and 155°. All the traces were downloaded from IRIS DMC database.

The estimated t^* parameters and the resulting coverage of the inner core are shown in Figure 2. The t^* parameter estimated by the *SAWIB* algorithm can assume discrete values between 0.04 and 4.08; these are the end values of the t^* parameter for compressional waves. Most of our t^* estimates are in the range between 0.04 and 1.2 s. There are, however, a number of larger estimates and a few observations having values on the order of 2 and 3 s. When these data are plotted on a scale encompassing the full range of estimated values, it is impossible to see the global variety of t^* parameters because of the majority of them plotting on the lower end of the color scheme, while a few larger values stand out in a drastically different color. We choose then to set the boundaries of our color scale to represent the range of the majority of our estimates, while those estimates that are larger than the ones shown are plotted in gray.

3. Transdimensional Algorithm

The transdimensional posterior probability distribution is defined by Bayes' theorem, which combines prior knowledge on the model $\mathbf{m}$ and the observed data $\mathbf{d}$:

$$p(\mathbf{m}|\mathbf{d}) \propto p(\mathbf{d}|\mathbf{m}) \times p(\mathbf{m}). \tag{1}$$

where $p(\mathbf{m}|\mathbf{d})$ means the probability of having $\mathbf{m}$, given or conditional on $\mathbf{d}$. The term $p(\mathbf{m})$ is called the *prior* probability distribution function (Prior PDF) of model parameters $\mathbf{m}$. It represents any knowledge that we have on the model before we measure the data (Tarantola, 2005). The Prior PDF is set up as uniform with bounds that encompass all possible values that a model parameter can assume. The likelihood function $p(\mathbf{d}|\mathbf{m})$ tells us how well a given set of model parameters explain the observed data. We assume that the errors on our t^* parameter are independently and normally distributed, which leads to a likelihood function of the following form:

$$L = p(\mathbf{d}|\mathbf{m}) = C \cdot \exp\left[-S(\mathbf{m})\right], \tag{2}$$

where $S(\mathbf{m})$ is given by

$$S(\mathbf{m}) = \frac{||\mathbf{G}(\mathbf{m}) - \mathbf{d}||_2^2}{2\sigma^2}, \tag{3}$$

where $||\cdot||_2$ is L_2 norm, $\mathbf{G}(\mathbf{m})$ is data predicted from model $\mathbf{m}$, $\mathbf{d}$ is the observed data, and σ^2 is data noise variance. $S(\mathbf{m})$ is measuring the deviation of the observed data from those predicted from model $\mathbf{m}$, and C is a constant. The model vector $\mathbf{m}$ is of variable dimension, and the complexity of the model is to be determined by the data. This differs from more "classic" optimization schemes, where the complexity of the model is fixed by the user in advance.

When the noise variance is known, the model that we are inverting for is given by $\mathbf{m} = [\mathbf{c}, \mathbf{Q}, n]$, where $\mathbf{c}$ is a vector of Voronoi cell nodes, $\mathbf{Q}$ is a vector of Q_p values assigned to each cell, and n is the number of Voronoi cells, which is itself variable. Since we are not inverting for depth layers, but rather assuming one approximately 400-km-thick layer of attenuation below the inner core boundary (ICB), vector $\mathbf{c}$ has only two components.

The algorithm follows the approach of Bodin and Sambridge (2009) and can be summarized as follows: at each iteration, for a given geometry of raypaths, the transdimensional algorithm produces a number

of Voronoi models (this number depends on the number of Markov chains) $\mathbf{m} = [\mathbf{c}, \mathbf{Q}, n]$ with variable dimensions from which Bayesian statistics can be computed. Each component of $\mathbf{m}$ is given a wide uniform distribution ensuring in this way that the models will be dominated by the data, rather than the prior assumptions. After the new Voronoi models have been computed, the reference model is updated by spatially averaging over the entire ensemble of models. Before the first step the reference model is laterally homogeneous model of Q_p. In this way, the algorithm essentially produces a sequence of random samples $\mathbf{m}$, each of which is a perturbation of the last, forming a chain. Upon convergence of the Markov chain these samples will be approximately distributed according to the transdimensional posterior probability distribution $p(\mathbf{m}|\mathbf{d})$. Sampling is based on a variation of the Metropolis-Hastings algorithm (Hastings, 1970; Metropolis, 1953), the reversible-jump Markov chain Monte Carlo (rj-MCMC) sampler (Green, 1995, 2003). Once the random walk is initiated, the algorithm guides the walk by the Metropolis-Hastings rule for transitions between models $\mathbf{m}$. This transition proposal from state i to state j is drawn from a proposal probability distribution $q(\mathbf{m_i}|\mathbf{m_j})$, such that the proposed model $\mathbf{m_i}$ is conditional only on the current model $\mathbf{m_j}$. The new model $\mathbf{m_i}$ drawn from distribution $q(\mathbf{m_i}|\mathbf{m_j})$ is accepted with probability $\alpha(\mathbf{m_i}|\mathbf{m_j})$. A uniform random deviate, r, is drawn between 0 and 1. If $r \leq \alpha$, the move is accepted, the current model $\mathbf{m_j}$ is replaced with new model $\mathbf{m_i}$, and the chain proceeds to the next step. If $r > \alpha$, the move is rejected and the current model is retained for the next iteration of the chain, where the process is repeated. The acceptance probability $\alpha(\mathbf{m_i}|\mathbf{m_j})$ is given by

$$\begin{aligned}\alpha(\mathbf{m_i}|\mathbf{m_j}) &= \min\left[1, \textbf{prior ratio} \times \textbf{likelihood ratio} \times \textbf{proposal ratio} \times |\mathbf{J}|\right] \\ &= \min\left[1, \frac{p(\mathbf{m_i})}{p(\mathbf{m_j})} \times \frac{p(\mathbf{d}|\mathbf{m_i})}{p(\mathbf{d}|\mathbf{m_j})} \times \frac{q(\mathbf{m_j}|\mathbf{m_i})}{q(\mathbf{m_i}|\mathbf{m_j})} \times |\mathbf{J}|\right]\end{aligned} \tag{4}$$

where the matrix $\mathbf{J}$ is the Jacobian of the transformation from $\mathbf{m_j}$ to $\mathbf{m_i}$, and it accounts for the difference in volume between two spaces of different dimension, or it can account for the transformation of two parameterizations with the same number of unknowns (Bodin & Sambridge, 2009; Green, 2003). For the problem considered here $|\mathbf{J}| = 1$ and it can be ignored (see the Appendix of; Bodin & Sambridge, 2009, for details). Once the model parameters are randomly initialized by drawing samples from the Prior PDF, the algorithm proceeds iteratively. Each step of the Markov chain has three stages:

1. Propose a new model from a proposal probability distribution $q(\mathbf{m_i}|\mathbf{m_j})$ such that the proposed model $\mathbf{m_i}$ is conditional only on the current model $\mathbf{m_j}$. This involves one, randomly chosen, type of change:
   (i) *Change a value of* Q_p: randomly choose a Voronoi cell from a uniform distribution and change its assigned Q_p value according to a Gaussian proposal probability distribution $q(Q_i|Q_j)$ centered on the current value Q_j. We use symmetric Gaussian proposals for change of value propositions and tune the standard deviation to achieve reasonable acceptance rates.
   (ii) *Move a Voronoi node*: randomly choose a Voronoi cell and perturb its node according to a spherical Von Mises probability distribution centered at the current position c_j.
   (iii) *Birth*: create a new Voronoi cell by randomly drawing a point on the 2-D sphere. The constant Q_p value for the new cell is sampled from the Prior PDF as this simplifies the acceptance criterion (equation (4)) for birth/death steps and has been shown to result in better acceptance rates for birth/death steps (see Dosso et al., 2014).
   (iv) *Death*: delete a Voronoi node randomly from the current set of n cells.
2. Compute t^* estimates for the proposed Voronoi model. These predicted estimates are compared to the observed ones to build the likelihood (equation (2)) and the posterior value of the proposed model $p(\mathbf{m}|\mathbf{d})$.
3. Randomly accept or reject the proposed model according to the acceptance criterion based on the Metropolis-Hastings rule (equation (4)).

The first part of the chain is discarded as a "burn-in" period after which the random walk is assumed to be stationary. The output distribution of the algorithm is thinned by including only every nth model in the ensemble to reduce unwanted correlation between samples within the chain.

When treating data noise as a variable, and running the algorithm hierarchically, the first stage of the Markov chain iterations has an additional, fifth, substep, which is changing the noise parameter. In this substep, the value of the noise parameter is randomly perturbed according to a Gaussian probability density centered at the current value of noise. One might expect the algorithm to choose higher values for data noise, as

this would reduce the misfit between the observed and predicted data. However, because of the natural parsimony associated with Bayesian inference this is not the case.

For more information and details on transdimensional algorithms and tomography the reader is referred to Mosegaard and Tarantola (1995), Bodin and Sambridge (2009), and Bodin et al. (2012).

4. Implementation of the Algorithm

4.1. Prior PDF

It is possible to use the algorithm in two ways: inverting for $\log(Q_p)$ and inverting directly for Q_p. We have explored both to see how the models differ. In each case we chose a uniform Prior PDF on all the parameters for both cases. This means that before considering the data, we assert that our knowledge of the parameter type, that is, either Q_p or $\log(Q_p)$, is equally likely to be anywhere between the respective bounds but not outside. Note that in choosing a uniform Prior PDF on different parameterizations, that is, on Q_p or $\log(Q_p)$, constitutes differing assumptions, which will likely influence the results. In our experiments the algorithm had difficulties converging when inverting directly for Q_p, so we do not present the results of the inversion for this case but we restrict ourselves to some speculation about what has occurred.

The bounds of the Prior PDFs differ depending on whether the inversion is run in log space or for Q_p directly. A uniform Prior PDF was chosen as we did not wish to bias our results toward some reference model for which we do not have good prior information. In the linearized inversion study of Pejić et al. (2017) a Gaussian Prior PDF allowed relatively small deviations from a central, reference, value. This prevented the solution model to acquire physically unrealistic (extremely high or low) values. In transdimensional Bayesian approach, however, we do not have the limitations of a fixed grid (i.e., a fixed number of parameters) or an explicit regularization term. The solution and its uncertainties depend predominantly on the data. Setting wide bounds on the uniform Prior PDF means, we consider all the values in between those bounds equally likely.

Since the algorithm is birthing from the Prior PDF, it will generate a cell with the value of Q_p between the lower and upper bound of the prior. For the case when parameters are Q_p (rather than $\log(Q_p)$), we set the lower bound to 0 and the upper bound to 1,000. Both of these values are extreme for the inner core, and we expect the estimates of Q_p to lie between those two values. So when birthing from the Prior PDF and inverting directly for Q_p, the algorithm will create a cell with a Q_p value chosen randomly between lower and upper bounds. A uniform Prior PDF in log space will result in a different prior on Q_p. The samples drawn from a uniform prior in log space will be distributed lognormally. Sampling in log space is therefore likely to be more efficient than sampling directly for Q_p, as the Prior PDF proposal width in log space will have the same proportional effect on both low and high values of Q_p. For example, if we sample directly for Q_p and the prior proposal width is 0.1, then for two different values of Q_p—say, 0.1 and 1000—we would get new values of 0.2 and 999.9 (since the maximum allowed value is 1,000). While the first value has doubled, the second has barely changed. In log space, the new proposed values are $\exp[\log(0.1) + 0.1] \approx 0.11$ and $\exp[\log(1000) - 0.1] \approx 900$, and both values have changed by the same relative amounts. So when sampling in log space, birthing from the Prior PDF will preferentially create a new cell with low Q_p values. For this reason, we have set the lower bound of the uniform prior in log space to 0, and the upper bound to 6.9, which is equivalent to $Q_p \approx 1,000$. The Prior PDF proposal width was adjusted on a case-to-case basis in order to achieve acceptance rates as close as possible to 50%. It is likely that this difference in proposals is affecting the rate of convergence of the algorithm and causing the aforementioned difficulties in convergence when inverting directly for Q_p.

4.2. Noise and Likelihood

Data noise variance σ (shown in equation (3)) is defined as a product of data noise σ_d and the scaling hierarchical parameter λ

$$\sigma = \sigma_d \cdot \lambda. \tag{5}$$

With this definition we can write the likelihood, equation (2), in the following form:

$$L = p(\mathbf{d}|\mathbf{m}) = C \cdot \exp\left[\frac{||\mathbf{p}(\mathbf{m}) - \mathbf{d}||_2^2}{2\sigma_d^2\lambda^2}\right]. \tag{6}$$

The negative logarithm of likelihood,

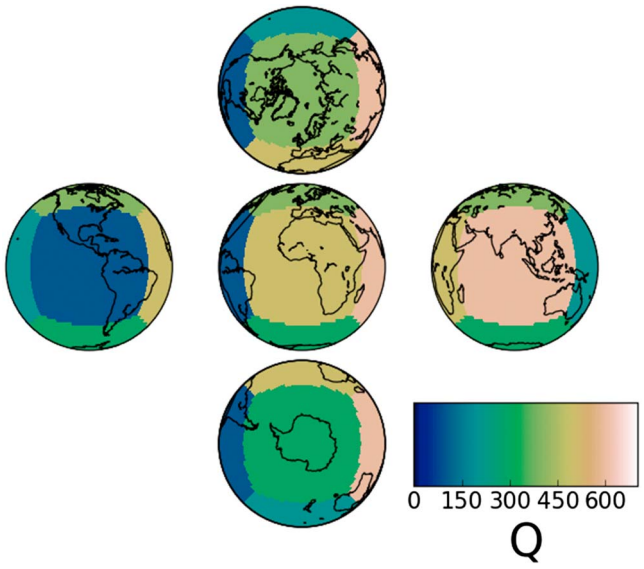

Figure 3. Cubed sphere input model for the synthetic tests. The model has six cells with Q_p value ranging from a 100 to 600 in steps of a 100. The image in the middle shows the model centered on the equator and the zeroth meridian. The images to its left and right are centered on the longitude of 270° and 90°, respectively, while the ones above it and below it are centered at the latitude of 90° and −90°, respectively. This allows to inspect the recovered model from various perspectives, including the polar ones.

$$-\log(L) = -\frac{||\mathbf{p}(\mathbf{m}) - \mathbf{d}||_2^2}{2\sigma_d^2\lambda^2} + C, \tag{7}$$

is a measure of data misfit. In synthetic tests we use data predicted from the model and add Gaussian noise to the data. For example, if we set the standard deviation of the Gaussian to ϵ, then any given predicted datum t_p^* is described as $t_p^* = t_i^* \pm \epsilon$, where t_i^* is raw predicted datum from the input model. In this case the value ϵ is the "true" value of noise in the synthetic data. When performing synthetic tests hierarchically, that is, when data noise is a parameter of the inversion, σ_d is fixed to value ϵ, while λ is allowed to change. We can see from equation (5) that if λ attains a value around 1.0, σ will be approximately equal to σ_d, which means the data noise is properly resolved.

When using the algorithm with real data t^*, we assume $\sigma_d = 1.0$ and again allow λ to change. Equation (5) tells us then that the estimated value of λ will be the estimate of actual noise σ in our data. We show the histograms for λ and taking its maximum as the noise estimate for hierarchically run algorithm in both synthetic and real data cases.

4.3. Inversion Details

In synthetic tests we used 9 Markov chains for 3 million steps each, while with real data 24 chains were used. We performed the inversion hierarchically, that is, treating the noise as a parameter of the inversion as described above. The maximum number of Voronoi cells allowed in the model was 200. This should be ample for our case, as we expect to not have the resolution scale lengths equivalent to much more than 30 cells in the model. The McMC algorithm produces dependent samples, that is, the next step is dependent on the last; however, our objective is to gather statistically independent samples. To encourage independent samples, it is best practice to discard the first steps in the chain, here we set at a million samples, and also "thin the chain," in our case by taking only every 100th model. Discarding these "burn-in" steps lets the chain "forget" where it started, and by thinning over a sufficient number of samples encourages independence. See Brooks et al. (2011) for detailed discussions

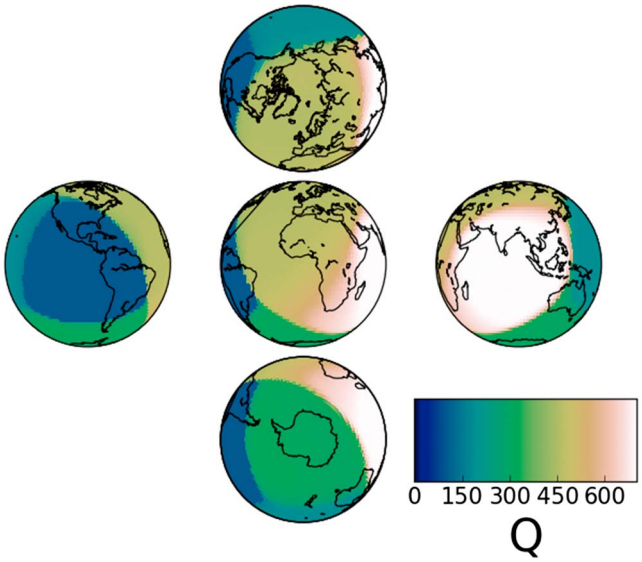

Figure 4. The recovered spatial median of 180,000 models in the synthetic example discussed in section 5, which compares well with the true cubed sphere model shown in Figure 3. The standard deviation of added Gaussian noise to predicted t^* values was $\sigma_d = 0.1$, and the inversion was performed with noise as a free parameter and using $\log(Q_p)$ as the model parameter. $Q_{p_{\min}} = 103$, $Q_{p_{\max}} = 731$. As expected, the recovery is commensurate with the raypath coverage shown in Figure 2.

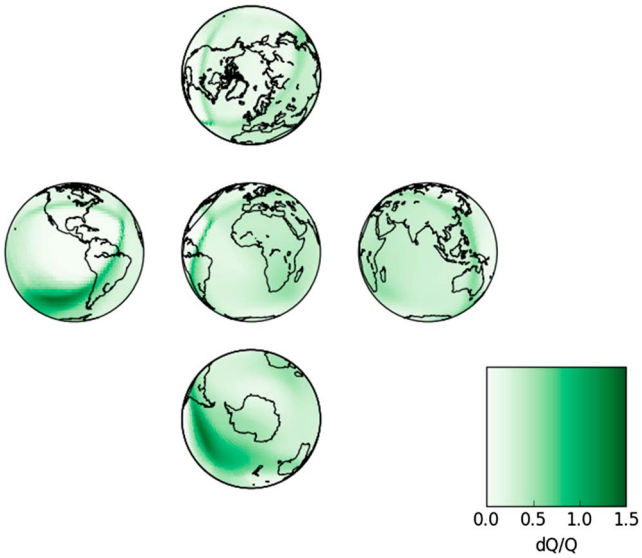

Figure 5. The dQ is the calculated standard deviation of the ensemble of attenuation models, and it is divided by the mean of the ensemble of attenuation models. Hence, the maps in the figure show a percentage of deviation of Q_p from its mean value for 180,000 models in the synthetic example for the cubed sphere input model shown in Figure 3. The standard deviation of added Gaussian noise to predicted t^* values was $\sigma_d = 0.1$. The inversion was performed with noise as a free parameter and using $\log(Q_p)$ as the model parameter.

on these issues. Since each step of the chain changes XX parameters and we have YY parameters every 100th step means that each parameter can in theory change KK times, and we make the assumption that this is sufficient to allow independence. For our case then this gives us 20,000 pseudo-independent models (samples) per chain. The collected output samples from all chains after burn-in is referred to as the "ensemble." We compute the necessary statistical moments of this ensemble and show its median and standard deviation in the figures below. We show the median of the ensemble because our Prior PDF has Q_p lognormally distributed.

5. Synthetic Tests

The input model for synthetic tests is a cubed sphere model shown in Figure 3. It has six cells with Q_p value ranging between a 100 and 600, in steps of a 100. The standard deviation of Gaussian noise added to predicted t^* values was $\sigma = 0.1$. We show the ensemble median and the uncertainty in Figures 4 and 5. The median of Q_p over the globe ranges from between 103 and 731. The uncertainty is computed by taking the standard deviation of the ensemble of recovered models and dividing by the mean value of the ensemble of the same models. This then gives us a percentage of deviation of the recovered attenuation Q_p from its mean value. As expected, this deviation is the highest around presumed Voronoi cell boundaries because the cells from differing models within the ensemble will create different overlaps, that is, the cells will not be exactly the same size and/or shape across every model in every chain. In the synthetic input model these boundaries are strictly given but are recovered with varying degrees of accuracy; hence, the biggest deviation of Q_p for a synthetic model is found along those boundaries.

In Figure 4 the color scale is clipped at the largest value shown—every value larger than the maximum of the color scale ($Q = 700$) is plotted in the colour of that maximum.

The histogram for number of cells is shown in Figure 6 and shows a maximum at the correct value of the input model, marked by vertical red line. The histogram for the scaling hierarchical parameter is shown in Figure 7. This last histogram shows a Gaussian distribution with a maximum frequency at 1.03, signifying well-sampled parameter space and well-recovered input noise. We can conclude from these tests that the recovery of the underlying model should be reasonably good. On average, however, beam focusing effects and underestimation of attenuation is likely in the Southeast Asia region.

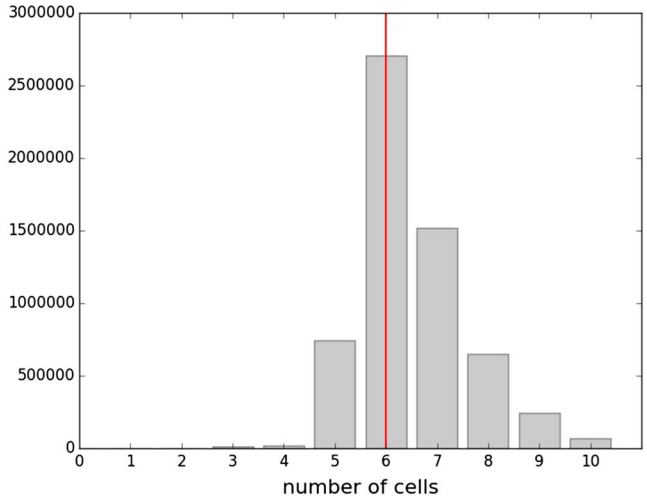

Figure 6. A histogram of recovered number of cells for the synthetic example of the CS model with $\sigma = 0.1$ of added Gaussian noise to predicted data, and noise is treated as a free parameter of the inversion. Recall that the initial number of cells is set to 6 (see Figure 3). The maximum is centered on the true number of cells in the input model, indicated by the red line. The histogram shows that the majority of the models recovered from synthetic data in this example have six cells representing a total of six different inner core attenuation regions. This coincides with the input synthetic CS model shown in Figure 3. CS = cubed sphere.

6. Results

Figures 8 and 9 show the ensemble median and the uncertainty for this case. The minimum and maximum values obtained for median Q_p are 47 and 643, respectively. As explained above in section 5, the uncertainty is computed by taking the standard deviation of the ensemble of recovered models and dividing by the mean value of the ensemble of the same models, which gives us the percentage of deviation of attenuation from its mean value. In this case, with real data, the boundaries between cells are not obvious as in the case of strictly imposed synthetic models, except around the region of the inner core beneath South America. The ring-like structures with large uncertainties that we observe around South America region are a consequence of Voronoi cell parameterization in transdimensional inversions. A characteristic of mobile

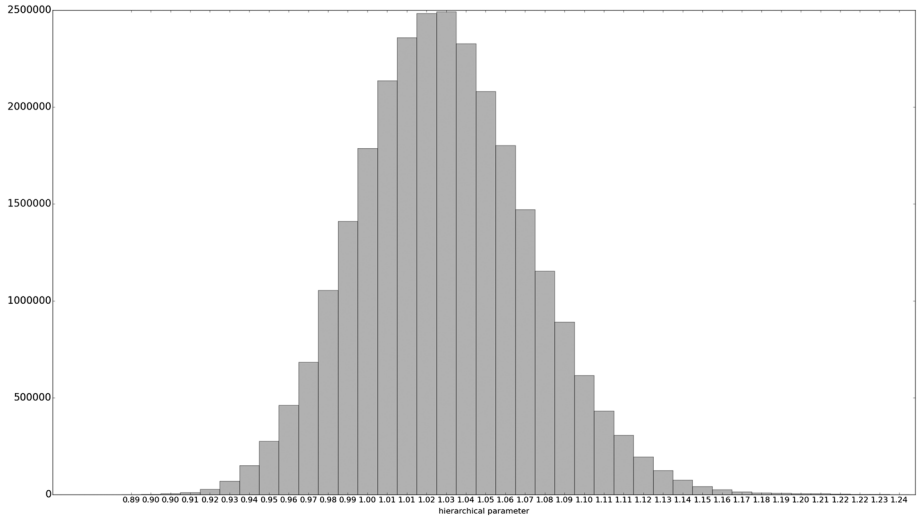

Figure 7. Histogram of the scaling hierarchical parameter for the synthetic data noise shows a Gaussian distribution with a maximum around 1.0 signifying well-sampled parameter space and correctly recovered input noise for the synthetic test. The reader is reminded that the noise σ is given by equation (5), and in the case of synthetic tests, the hierarchical parameter λ equal to 1.0 indicates well-recovered noise added to the synthetic data. Section 4.2 provides detailed explanation on treatment of data noise in the inversion.

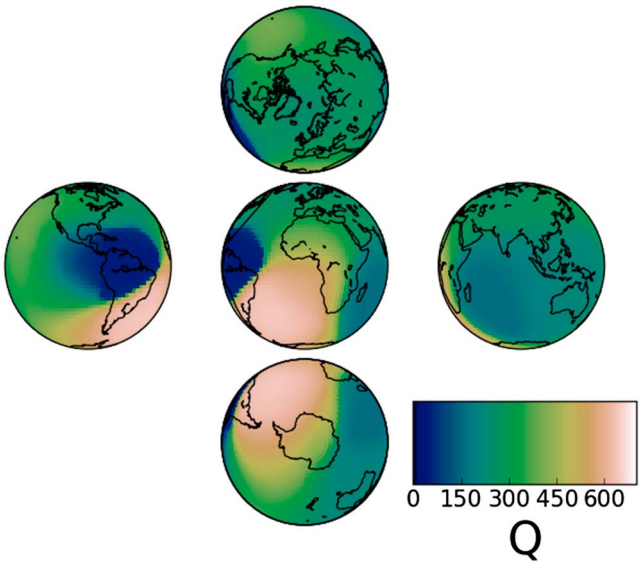

Figure 8. Ensemble median of Q_p for the upper inner core. The inversion was performed with data noise σ as a free parameter and using $\log(Q_p)$ as the model parameter. $Q_{p_{\min}} = 47$, $Q_{p_{\max}} = 643$.

Voronoi cells is that they produce regions of multimodal posteriors, which results in the ring-like structures of large magnitude in posterior standard deviation (Hawkins et al., 2018). The histogram of recovered number of cells for this ensemble has a maximum at 7 (Figure 10). This histogram also shows no models with number of parameters greater than 22, which is fewer than in the fixed parameterization used by Pejić et al. (2017). This smaller number of parameters makes sense, given the sparse coverage of our data set. Histogram in Figure 11 shows that the hierarchical parameter, equivalent to estimated noise, has a maximum at $\sigma = 0.36$. This value is in good agreement with values estimated from the L-curve and the Discrepancy Principle performed by Pejić et al. (2017), where they were 0.17 and 0.38, respectively.

Low attenuation is observed in the region of the inner core beneath the Atlantic and Africa, and high attenuation is observed in the regions beneath the Indian ocean, Southeast Asia, and Australia. This attenuation

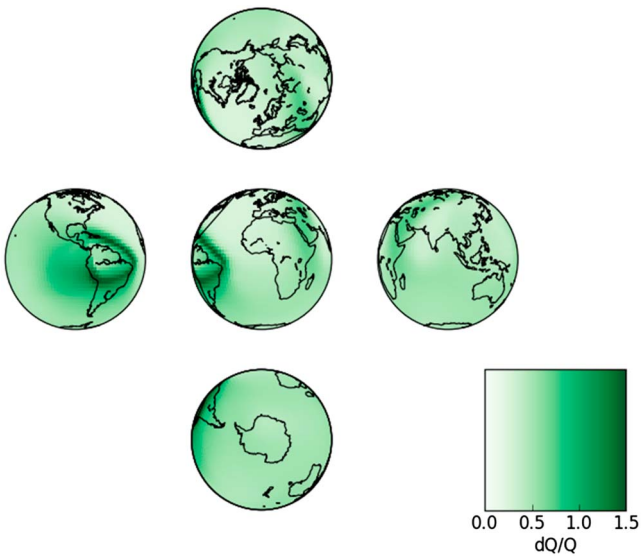

Figure 9. The dQ is the calculated standard deviation of the ensemble of attenuation models, and it is divided by the mean of the ensemble of attenuation models. Hence, the maps in the figure show a percentage of deviation of Q_p from its mean value for the ensemble of attenuation models. The inversion was performed with data noise σ as a free parameter and using $\log(Q_p)$ as the model parameter.

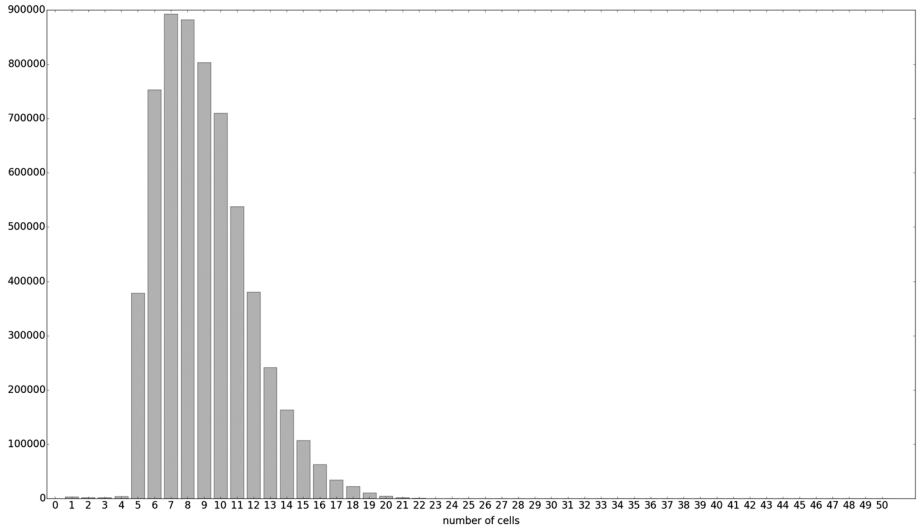

Figure 10. Histogram for number of cells in the ensemble of models for Q_p of the upper inner core. The inversion was performed with data noise σ as a free parameter and using $\log(Q_p)$ as the model parameter. The maximum of the histogram is centered on seven cells, signifying that the majority of the models recovered in the inversion have seven cells (seven distinct values of Q_p recovered).

is only slightly lower in the inner core below the western Pacific and then increases again and is the highest beneath Central America. Again, we observe an anomalously high attenuation in some regions of the inner core beneath South America. While such a low Q_p seems highly unlikely in the inner core, all these results potentially point to a significantly higher attenuation in that region than anywhere else in the core. Additionally, we also observe higher uncertainties in that region. Hawkins et al. (2018) pointed out that while discontinuities in the 2-D field in the transdimensional inversion will lead to large standard deviation, the large standard deviation does not necessarily imply discontinuities in the field. The region of the inner core beneath South America requires further study and measurements in order to establish whether there potentially exists a prominent discontinuity of attenuation in that part of the inner core. Overall, the results obtained from transdimensional inference are in a good agreement with the ones obtained from linearized inversion in Pejić et al. (2017).

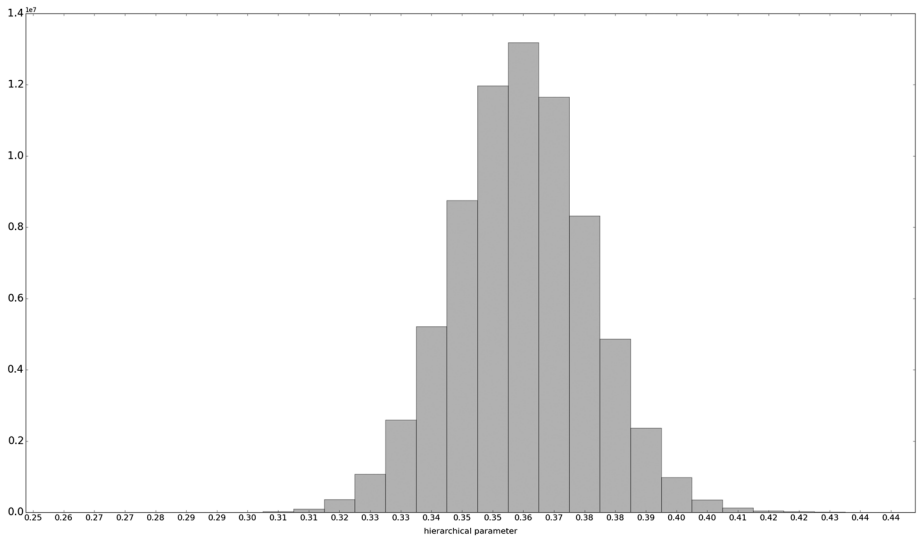

Figure 11. A histogram of hierarchical parameter, equivalent to estimated data noise σ, shows a maximum at $\sigma = 0.36$. The inversion was performed using $\log(Q_p)$ as the model parameter. Data noise is defined in equation (5). For inversion runs with real data the quantity σ_d in equation (5) is set to 1.0; hence, the hierarchical scaling parameter λ is then an estimate of real data noise.

7. Discussion and Interpretation

Our results consistently show high inner core attenuation in the region beneath Asia, the Indian Ocean, and Australia, with slightly lower attenuation extending over the region beneath Pacific and then again reaching its peak in the region beneath Central America and northern parts of South America. We observe low inner core attenuation beneath the South Atlantic and most of Africa. Transdimensional inference points to lower attenuation in the regions beneath Antarctica, and slightly higher attenuation beneath the North Pole; however, we refrain from interpreting these areas because we have limited coverage there.

Over the past years various geodynamical scenarios have been proposed to explain seismic observations, both in compressional velocity in the inner core and observed attenuation (see Tkalčić, 2017, for extensive discussion). Interpretations have specifically been focused on the apparent hemispherical structure observed since the early nineties. Most of these mechanisms highlight different areas of the presumed crystallization of the ICB and the effect of the crystallization rate on the porosity of medium forming the topmost part of the inner core. Porosity is defined as the ratio of the volume of void space (e.g., liquid inclusions) in the material and the total bulk volume of the material. Permeability will be high for well connected liquid inclusions and low for well isolated liquid inclusions with many boundaries between them.

According to Sumita and Olson (1999) cold and warm fronts develop in the outer core, leading to a rapid crystallization on the cold, western, side of the inner core. Higher porosity was argued to produce a material with lower compressional velocity. If that scenario is true, then faster crystallization rate results in higher porosity presumably trapping the liquid inclusions in their initial state and not providing enough time for isolating boundaries to form. Higher porosity also causes lower compressional velocity and lower attenuation, as the propagating waves will travel through less dense material and slow down, and at the same time interact with fewer material boundaries and lose less energy through scattering. In order for this scenario to explain the previous seismic observation of lower velocities and lower attenuation in the quasi-western hemisphere (qWH) and higher velocities and higher attenuation in the quasi-eastern hemisphere (qEH) of the inner core, one must conclude that the qWH crystallizes faster and is colder than the qEH. In light of this mechanism our attenuation results point to fast crystallization over Southeast Asia, the Indian Ocean, and Australia, and potentially even higher rate of crystallization beneath the Central America and northern parts of South America. This would imply highly porous material beneath Atlantic and Africa, and less porous material with smaller grains beneath the belt covering Asia-Pacific, which agrees with the study of Stroujkova and Cormier (2004).

Aubert et al. (2008) propose a different mechanism of crystallization and grain formation by coupling the ICB to the thermal anomalies of the lowermost mantle. According to their models thermal flow through the outer core (OC) is dominated by wide downwelling and upwelling cyclones. The center feature of their model is a cold, downwelling cyclone beneath Southeast Asia, bringing cold fluid to the ICB. It is speculated that this is the region of fastest growth (fastest crystallization) and formation of well-isolated liquid inclusions and more randomly spaced dendrites. This is the opposite mechanism to the one suggested by Sumita and Olson (1999). Here we have formation of less porous material through fast crystallization while Sumita and Olson (1999) proposed the other way around. So according to the model of Aubert et al. (2008) it is the qEH that crystallizes faster and is colder than the qWH, which is the opposite conclusion form the one reached following the mechanism of Sumita and Olson (1999). The mechanisms explaining seismic observations of velocities and attenuation are nevertheless the same; however, they predict different dynamics for the two hemispheres of the inner core. Gubbins et al. (2011) also conclude that qEH crystallizes faster, but their models assume narrow downwellings and widespread upwellings in the OC, and the ICB is a permeable boundary, allowing the heat flow to go to and from the IC. This scenario explains the *F* layer at the bottom of the OC and induces partial melting in the areas affected by downwelling hot fluid but otherwise predicts a similar scenario to the one by Aubert et al. (2008) in terms of the hemispheres. The big difference is that this model does not require the ICB to be locked to the thermal anomalies of the lowermost mantle.

The classic view of the inner core hemispherical structure (of isotropic velocity) has its roots in the early work of Shearer and Toy (1991), who described the pattern observed in the differential travel times of PKPbc and PKIKP waves as a manifestation of aspherical symmetry in inner core structure. Later work by Niu and Wen (2001) focusing on differential travel times of PKiKP and PKIKP waves confirmed hemispherical dichotomy. Although differential PKiKP and PKIKP travel time can only reach down to about 85 km beneath the inner

core surface, this is to date, arguably, the best constrained inner core-sensitive data set, which convincingly confirms that hemispherical dichotomy of the uppermost inner core.

It is worth noting that our results do not conform to the classic view of the hemispheres. On the contrary, we observe high attenuation in the qEH and it extends all the way through most of the qWH hemisphere. It is only a small part of the qWH, namely, beneath Atlantic and Africa where the observed attenuation is lower. In that sense, our observations support both of the above scenarios—fast crystallization in the qEH, beneath southeast Asia, Australia, and eastern Pacific, and potentially even higher crystallization rate in one part of the qWH, beneath parts of the western Pacific and Central and South America. What this means for grain formation and porosity of the material is unclear and beyond the scope of this study.

Monnereau et al. (2010) and Alboussière et al. (2010) propose an eastward translation of the material in the IC. This translation creates a positive ICB topography in the qEH and negative topography in the qWH. The qEH thus experiences melting, a phase change acting to reduce the excess topography, while qWH experiences crystallization acting to add to the reduced topography. This means the presence of large grains (on the order of several kilometers) in the qEH and small grains (on the order of hundreds of meters) in the qWH. This scenario is the exact opposite of the one suggested by Aubert et al. (2008) and Gubbins et al. (2011). In that scenario our results would mean melting and formation of large grains in the Asia-Pacific belt, and crystallization and formation of small grains below Africa and Atlantic. The downside of this model proposed by Monnereau et al. (2010) and Alboussière et al. (2010) is that convection in the IC depends entirely on its viscosity and thermal conductivity. Convection requires an inner core viscosity of more than 10^{18} Pa s (Deguen et al., 2013), which is several orders of magnitude larger than the current reported values (Deuss, 2014, and references therein). In addition, Pozzo et al. (2014) have modeled the electrical and thermal conductivity of pure iron and two iron-silicon solid solutions matching the seismically determined ICB density jump at the temperature and pressure conditions of the Earth's inner core. They found that the thermal conductivity is almost 4 times larger than the highest values currently in use, making the thermal diffusion time comparable to estimates of the inner core age. Their simple calculation appropriate to the early Earth shows the inner core to be thermally stable unless a core-mantle boundary (CMB) heat flux 3–5 times higher than present-day estimates could be sustained at the time. This means that the convection (and translation, being a mode of convection) is highly unlikely. Their calculations suggest that thermal convection in the inner core was unlikely even in its earlier stages.

Gomi and Hirose (2015) reached a similar conclusion by measuring the electrical resistivity of iron-nickel alloys in a diamond-anvil cell up to 70 GPa and 300 K. They use their calculated values to estimate the isentropic heat flow at the top of the inner core. The heat flow at the topmost outer core was estimated to be 13.9 and 10.9 TW for high and low CMB temperatures, respectively, which is in line with the CMB heat flow of 5–15 TW estimated from the mantle side (Gomi & Hirose, 2015, and references therein). In order for thermal convection to occur without compositional buoyancy, the CMB heat flow must exceed the isentropic heat flow at the top of the outer core mentioned above. Recognizing that ICB heat flow is equivalent to secular cooling of the inner core, they then calculated the CMB heat flow from energy balance of the core and found that the obtained CMB heat flow is 38.3 TW and 31.2 TW for high and low temperature cases, respectively. These values are significantly larger than recent 5- to 15-TW range. All of this suggests that the thermal conduction is sufficiently strong to suppress the thermal convection in the present-day inner core. However, recently, Gubbins et al. (2013) performed numerical evaluations of partitioning of oxygen, sulfur, and silicon in binary iron alloys and found that partition coefficients decrease with temperature, leading to a lowering of the concentration of light elements with radius in the inner core. This results in an unstable density gradient that is weak but strong enough to produce convection in the inner core, including the translational mode.

While not studied here, seismic anisotropy is a clear observed signal, which can provide us with additional constraints on possible geodynamical scenarios of the inner core. The inner core consists of large number of crystals which can only appear anisotropic if they are aligned in the same direction. There are two possible regimes for this alignment to happen (see, e.g., review by Bergman, 2003; Tkalčić & Kennett, 2008; Tkalčić, 2017, and references therein): solidification texturing and deformation texturing. In the solidification texturing regime one possibility is the alignment with the magnetic field; however, it is unclear whether this field is strong enough to produce said alignment. The other scenario is that the solidification of the inner core creates dendritic crystal structures aligned with the flow in the outer core. If the fast axis of the

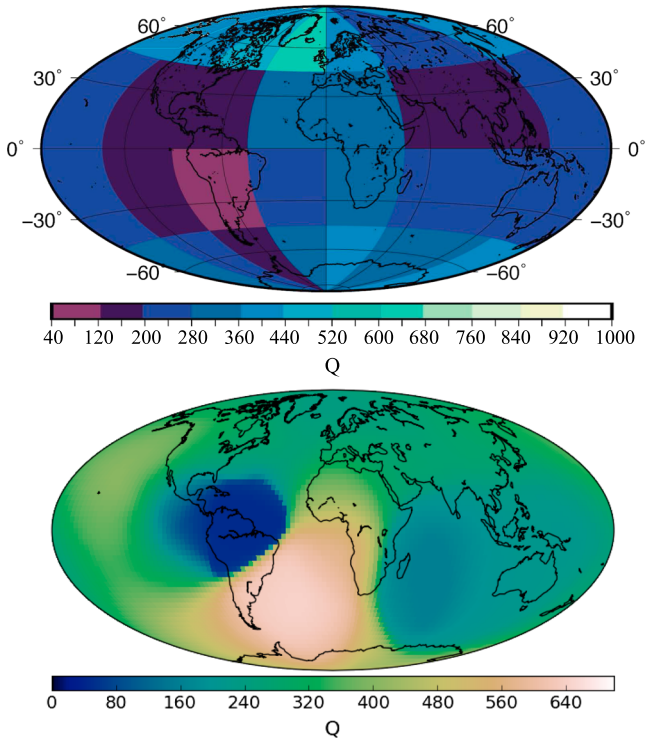

Figure 12. Final attenuation models from the linearized inversion of Pejić et al. (2017; top) and this study (bottom) shown on the same projection for easier comparison.

crystals is aligned with the rotation axis, then the outer core flow extracts more heat at the equator, which in turn results in the formed dendrites aligning in the equatorial plane. This model explains the increase in anisotropy with depth, and the attenuation anisotropy observed with body waves.

The deformation texturing after solidification regime offers three different mechanisms: (1) thermal convection, which, as we have just seen, is unlikely (Gomi & Hirose, 2015; Pozzo et al., 2014) but possible (Gubbins et al., 2013); (2) deformation by the Maxwell stress of the magnetic field, which aligns the fast axis parallel to the equator and cannot explain the anisotropy where fast axis is along the rotation axis; and (3) predominant growth of the inner core at the equator, which would result in radial anisotropy that would appear isotropic to body waves and explain the isotropic layer at the top of the inner core, but not the deeper anisotropy of the inner core. It is possible that some of these different mechanisms may be operating at the same time in different regions of the inner core.

If we are, however, looking for the simplest interpretation of our results, then in order to keep in line all of the above studies we can point out that our attenuation observations point to solidification of the inner core structures aligned with the flow in the outer core. This leads us back to the models proposed by Aubert et al. (2008) and Gubbins et al. (2011), and fast rate of crystallization beneath the Indian Ocean and Southeast Asia and possibly even higher rate of crystallization beneath Central America and western Pacific. Our results agree well with those of Attanayake et al. (2014), Iritani et al. (2014), and Iritani et al. (2014) who observed a similar pattern, and the assumption of solidification texturing aligned with the flow in the outer core accounts for the observed seismic anisotropy.

8. Conclusions

We performed transdimensional Bayesian inversion of attenuation data, using Voronoi cells defined on a spherical surface of uniform thickness. The result of one such inversion is an ensemble, in our case, of 4.8 million models (20,000 samples per chain, and 24 chains) of attenuation parameter Q_p, from which we obtained the relevant statistical moments. Histograms for number of Voronoi cells in the model and for the hierarchical parameter provide us with an estimate of model complexity and noise in the data, respectively. Our results support multiple implications for the structure and dynamics of the inner core. The reader is

reminded that we did not account for depth changes of attenuation in our algorithm, simply because we do not have enough well-distributed observations to make any assumptions about the depth dependence. The results shown and discussed in this study should be interpreted as an average lateral attenuation of ≈ 400-km-thick layer within the inner core.

One clear observation in our solutions is their difference from the widely accepted hemispherical attenuation structure with boundaries defined as in Tanaka and Hamaguchi (1997) and later studies (e.g., Waszek & Deuss, 2013). These boundaries extend from 44°E to 177°E for the Eastern and from 183°W to 43°E for the Western Hemispheres, and they were first reported for travel time anomalies, but later accepted for attenuation as well (e.g., Cao & Romanowicz, 2004; Wen et al., 2002). Our own results do not support these boundaries. Results from linearized (Pejić et al., 2017) and transdimensional inversion are reproduced here using the same projections for easier comparison in Figure 12. We observe a high attenuation in what was previously considered to be the eastern hemisphere, and this is in agreement with early studies of inner core attenuation. However, what was considered to be the Western Hemisphere is clearly more complex. In early studies this was presented as a region of low attenuation throughout but we can see in our results that the attenuation reaches its peak over the western Pacific and parts of Central and South America. It also reaches its low in that selfsame Western Hemisphere just beneath the Atlantic and Africa. So we can divide the "Western Hemisphere" into two regions: one with high attenuation and the other with low attenuation. This type of pattern is in agreement with the studies of Attanayake et al. (2014), Iritani et al. (2014), and Iritani et al. (2014). Our results are specifically in agreement with Figure 4 of Iritani et al. (2014), when one takes into account the depth extent of our data set, which approximately covers the middle third of the depth extent of their models for three regions within the inner core. Our tomograms are therefore providing a perspective on the inner core structure different from the purely hemispherical one. We should be cautious when interpreting the extremely high attenuation beneath Central and South America, as the Q_p factor for that region is uncharacteristically low. It is possible that this part of the solution is influenced by a few large t^* estimates that then control the inversion process and that removing them would result in lower attenuation in that region. The *SAWIB* algorithm used to estimate the t^* parameters uses ray theory and can potentially overestimate measurements on diffracted waves. We have, however, visually inspected all of the waveform fits and carefully selected the ones we used for data points. Furthermore, transdimensional inversion provides a more realistic estimate of the uncertainties, computed from the models within the ensemble. Therefore, we have no reasons to disregard the high attenuation beneath Central America as a valid inference. Our results are supportive of the role the lowermost mantle plays in mapping the thermal features onto the inner core surface, through the flow within the outer core.

Acknowledgments
The authors wish to thank the Editor and three anonymous reviewers for their constructive comments and suggestions. Some calculations were performed on the Terrawulf cluster, a computational facility supported through the AuScope Australian Geophysical Observing System (AGOS) and the National Collaborative Research Infrastructure Strategy (NCRIS), both Australian Federal Governments programs. Pejic and Hawkins thank the Australian National University for IPRS and APA scholarships that made this research possible. The seismograms used in this study were downloaded from IRIS DMC database (ds.iris.edu). The previous study (Pejić et al., 2017) lists events used in Appendix A, and network codes of all station operators in the Acknowledgments section. The t^* data obtained through the use of the *SAWIB* algorithm, final attenuation model, and the transdimensional inversion software used in this study can all be found at Hawkins' github repository (https://github.com/rhyshawkins/AttenuationVoronoi).

References

Alboussière, T., Deguen, R., & Melzani, M. (2010). Melting-induced stratification above the Earth's inner core due to convective translation. *Nature*, *466*, 744–747.

Attanayake, J., Cormier, V. F., & de Silva, S. M. (2014). Uppermost inner core structure—New insights from body waveform inversion. *Earth and Planetary Science Letters*, *385*, 49–58. https://doi.org/10.1016/j.epsl.2013.10.025

Aubert, J., Amit, H., Hulot, G., & Olson, P. (2008). Thermochemical flows couple the Earth's inner core growth to mantle heterogeneity. *Nature*, *454*, 758–761.

Backus, G., & Gilbert, F. (1968). The resolving power of gross Earth data. *Geophysical Journal of the Royal Astronomical Society*, *16*, 169–205.

Bergman, M. I. (2003). Solidification of the Earth's core. In V. Dehant, K. C. Creager, S.-I. Karato, & S. Zatman (Eds.), *Earth's core: Dynamics, structure, rotation*. Washington, DC: American Geophysical Union. https://doi.org/10.1029/GD031p0105

Bodin, T., & Sambridge, M. (2009). Seismic tomography with the reversible jump algorithm. *Geophysical Journal International*, *178*(3), 1411–1436.

Bodin, T., Sambridge, M., Rawlinson, N., & Arroucau, P. (2012). Trans-dimensional tomography with unknown data noise. *Geophysical Journal International*, *189*, 1536–1556.

Brooks, S., Gelman, A., Jones, G. L., & Meng, X. (2011). *Handbook of Markov Chain Monte Carlo*. London: Chapmann & Hall/CRC.

Cao, A., & Romanowicz, B. (2004). Hemispherical transition of seismic attenuation at the tope of the Earth's inner core. *Earth and Planetary Science Letters*, *28*, 243–253. https://doi.org/10.1016/j.epsl.2004.09.032

Deguen, R., Alboussière, T., & Cardin, P. (2013). Thermal convection in Earth's inner core with phase change at its boundary, Geophysical Journal International. *194(3)*, 1310–1334. https://doi.org/10.1093/gji/ggt202

Dettmer, J., Dosso, S. E., & Holland, C. W. (2010). Trans-dimensional geoacoustic inversion. *The Journal of the Acoustic Society of America*, *128*(6), 3393–3405.

Deuss, A. (2014). Heterogeneity and anisotropy of Earth's inner core. *Annual Review of Earth and Planetary Sciences*, *42*, 103–126.

Dosso, S. E., Dettmer, J., Steininger, G., & Holland, C. W. (2014). Efficient trans-dimensional Bayesian inversion for geoacoustic profile estimation. *Inverse Problems*, *30*(11), 114018. https://doi.org/10.1088/0266-5611/30/11/114018

Garcia, R., Shardong, L., & Chevrot, S. (2013). A nonlinear method to estimate source parameters, amplitude, and travel times of teleseismic body waves. *Bulletin of the Geological Society of America*, *103*, 268–282.

Gomi, H., & Hirose, K. (2015). Electrical resistivity and thermal conductivity of hcp Fe–Ni alloys under high pressure: Implications for thermal convection in the Earth's core. *Physics of the Earth and Planetary Interiors*, *247*, 2–10.
Green, P. (1995). Reversible jump MCMC computation and Bayesian model selection. *Biometrika*, *82*, 711–732.
Green, P. (2003). Trans-dimensional Markov Chain Monte Carlo. *Highly Structured Stochastic Systems*, *27*, 179–198.
Gubbins, D., Alfè, D., & Davies, C. J. (2013). Compositional instability of Earth's solid inner core. *Geophysical Research Letters*, *40*, 1084–1088. https://doi.org/10.1002/grl.50186
Gubbins, D., Sreenivasan, B., Mound, J., & Rost, S. (2011). Melting of the Earth's inner core. *Nature*, *473*, 361–364.
Hastings, W. (1970). Monte Carlo simulation methods using Markov chains and their applications. *Biometrika*, *57*, 97–109.
Hawkins, R., Bodin, T., Sambridge, M., Choblet, G., & Husson, L. (2018). Trans-dimensional surface reconstruction with different classes of paramaterization. *Geochemistry, Geophysics, Geosystems*, *20*. https://doi.org/10.1029/2018GC008022
Iritani, R., Takeuchi, N., & Kawakatsu, H. (2014). Intricate heterogeneous structures of the top 300 km of the Earth's inner core inferred from global array data: I. Regional 1D attenuation and velocity profiles. *Physics of the Earth and Planetary Interiors*, *230*, 15–27. https://doi.org/10.1016/j.pepi.2014.02.002
Iritani, R., Takeuchi, N., & Kawakatsu, H. (2014). Intricate heterogeneous structures of the top 300 km of the Earth's inner core inferred from global array data: II. Frequency dependence of inner core attenuation and its implication. *Earth and Planetary Science Letters*, *405*, 231–243. https://doi.org/10.1016/j.epsl.2014.08.038
Mackay, D. (2003). *Information theory, inference, and learning algorithms*. Cambridge: Cambridge University Press.
Malinverno, A. (2002). Parsimonious Bayesian Markov chain Monte Carlo inversion in a nonlinear geophysical problem. *Geophysical Journal International*, *151*(3), 675–688.
Malinverno, A., & Briggs, V. A. (2004). Expanded uncertainty quantification in inverse problems: Hierarchical Bayes and empirical Bayes. *Geophysics*, *69*(4), 1005–1016. https://doi.org/10.1190/1.1778243
Metropolis, N. (1953). Equations of state calculations by fast computational machine. *The Journal of Chemical Physics*, *21*(6), 1087–1091.
Monnereau, M., Calvet, M., Margerin, L., & Souriau, A. (2010). Lopsided growth of Earth's inner core. *Science*, *328*, 1014–1017.
Mosegaard, K., & Tarantola, A. (1995). Monte Carlo sampling of solutions to inverse problems. *Journal of Geophysical Research*, *100*(B7), 12,431–12,447.
Niu, F., & Wen, L. (2001). Hemispherical variations in seismic velocity at the top of the Earth's inner core. *Nature*, *410*, 1081–1084.
Pejić, T., Tkalčić, H., Cormier, V. F., Sambridge, M., & Benavente, R. (2017). Attenuation tomography of the upper inner core. *Journal of Geophysical Research: Solid Earth*, 3008–3032. https://doi.org/10.1002/2016JB013692
Pozzo, M, Davies, C., Gubbins, D., & Alfé, D. (2014). Thermal and electrical conductivity of solid iron and iron silicon mixtures at Earth's core conditions. *Earth and Planetary Science Letters*, *393*, 159–164.
Sambridge, M., Gallagher, K., Jackson, A., & Rickwood, P. (2006). Trans-dimensional inverse problems, model comparison and the evidence. *Geophysical Journal International*, *167*(2), 528–542. https://doi.org/10.1111/j.1365-246X.2006.03155.x
Sambridge, M., & Rawlinson, N. (2005). Seismic tomography with irregular meshes. In A. Levander & G.Nolet (Eds.), *Seismic Earth: Array analysis of broadband seismograms* (pp. 49–65). Washington, DC: American Geophysical Union. https://doi.org/10.1029/157GM04
Shearer, P. M., & Toy, K. M. (1991). PKP(BC) versus PKP(DF) differential travel times and aspherical structure in the Earth's inner core. *Journal of Geophysical Research*, *96*(B2), 2233–2247. https://doi.org/10.1029/90JB02370
Stroujkova, A., & Cormier, V. F. (2004). Regional variations in the uppermost 100 km of the Earth's inner core. *Journal of Geophysical Research*, *109*, B10307. https://doi.org/10.1029/2004JB002976
Sumita, I., & Olson, P. (1999). A laboratory model for convection in Earth's inner core driven by a thermally heterogeneus mantle. *Science*, *274*(5294), 1883–1887.
Tanaka, S., & Hamaguchi, H. (1997). Degree one heterogeneity and hemispherical variation of anisotropy in the inner core from PKP(BC)-PKP(DF) times. *Journal of Geophysical Research*, *102*, 2925–2938. https://doi.org/10.1029/96JB03187
Tarantola, A. (2005). *Inverse problem theory and methods for model parameter estimation*. Philadelphia: Siam.
Tkalčić, H. (2017). The Earth's inner core revealed by observational seismology. Cambridge University Press.
Tkalčić, H., & Kennett, B. L. N. (2008). Core structure and heterogeneity: A seismological perspective. *Australian Journal of Earth Sciences*, *55*, 419–431.
Waszek, L., & Deuss, A. (2013). A low attenuation layer in the Earth's uppermost inner core. *Geophysical Journal International*, *195*(3), 2005–2015. https://doi.org/10.1093/gji/ggt368
Wen, L., Niu, F., & ESE 2-1 ESE 2-13 (2002). Seismic velocity and attenuation structures in the top of the Earth's inner core. *Journal of Geophysical Research*, *107*(B11). https://doi.org/10.1029/2001JB000170
Young, M. K., Tkalčić, H., Bodin, T., & Sambridge, M. (2013). Global *P* wave tomography of Earth's lowermost mantle from partition modeling. *Journal of Geophysical Research: Solid Earth*, *118*, 5467–5486. https://doi.org/10.1002/jgrb.50391